AIAA GNC/AFM/MST/ASC/ASE 2010 Conference **2010-8416**
2-5 Aug 2010, Toronto, Ontario, Canada

Determining Aerodynamic Characteristics of a Micro Air Vehicle Using Motion Tracking

Daniel V. Uhlig,* Agrim Sareen,† Pritam Sukumar,‡ Arjun H. Rao,§ and Michael S. Selig¶

University of Illinois at Urbana-Champaign, Urbana, IL 61801, USA

Measuring flight characteristics of micro-UAVs is challenging because of their small size and low weight. These constraints prevent the use of conventional on-board measurement systems. The objective of this research was to capture the state information of a radio controlled (RC) airplane using an off-board motion tracking system and to use this state information to study the performance of the airplane. The airplane used has a 37.5-cm (14.75-in) wingspan, weighs 11.5-g (0.41-oz), and has throttle, elevator and rudder control. Using the motion track, a time history of the position and attitude was recorded. This paper presents methods that were developed and implemented to calculate aerodynamic properties from the position and attitude tracking data. The lift and drag were estimated using data from uncontrolled glides and compared to predictions from thin airfoil theory. The state information was captured over multiple flight tests in order to study the airplane performance across various flight regimes.

Nomenclature

a_x, a_y, a_z	=	body-axis translational acceleration
$\mathcal{AR}$	=	aspect ratio
C_D	=	coefficient of drag
C_{D_o}	=	parasite drag
C_L	=	coefficient of lift
C_{L_α}	=	airplane lift curve slope
C_{l_α}	=	airfoil lift curve slope
C_l, C_m, C_n	=	roll, pitch, and yaw coefficients
D	=	drag
e_o	=	Oswald efficiency factor
$\mathbf{F}$	=	force
I_{xx}, I_{yy}, ...	=	mass moments of inertia
L	=	lift
m	=	airplane mass
p, q, r	=	roll, pitch and yaw rates
$\mathbf{R}$	=	transformation or rotation matrix
u, v, w	=	body-fixed translational velocity

*Graduate Student (Ph.D.), Department of Aerospace Engineering, 104 S. Wright St., AIAA Student Member.
†Graduate Student (M.S.), Department of Aerospace Engineering, 104 S. Wright St.
‡Graduate Student (Ph.D.), Department of Aerospace Engineering, 104 S. Wright St., AIAA Student Member.
§Graduate Student (M.S.), Department of Aerospace Engineering, 104 S. Wright St., AIAA Student Member.
¶Associate Professor, Department of Aerospace Engineering, 104 S. Wright St., Senior Member AIAA.
http://www.ae.illinois.edu/m-selig

V	=	inertial speed
α	=	angle of attack
β	=	sideslip angle
δ_e, δ_r	=	elevator and rudder deflections
ϕ, θ, ψ	=	roll, pitch and heading angles
ω	=	angular rates

Subscripts

ac	=	aircraft
b	=	body-fixed frame
cs	=	control surface
G	=	due to gravity
x, y, z	=	body-fixed axis system directions
E	=	earth-fixed axis system

I. Introduction

Very small airplanes with wingspans less than 50 cm (20 in) and weighing less 100 g (3.5 oz) are starting to become readily available and present a new opportunity for micro unnammed aerial vehicles (UAVs) to be used. Aerodynamics of very small aircraft are different from the better understood problem of larger UAVs. First, micro-UAVs fly at much lower Reynolds number. Second, due to structural efficiencies, the ratio between inertial, gravitational and aerodynamic forces is different from those of larger aircraft. Finally, small aircraft often fly over a larger range of angles of attack to increase maneuverability to operate within confined spaces. In order to better understand the aerodynamics of micro-UAVs, flight measurements are needed.

A study by Mettler of a micro-UAV in free-flight used a small 2-g (0.07-oz) glider to investigate micro-scale aerodynamics.[1,2] The small free flight glider was hand launched and not controlled. From the trajectory data, basic aerodynamic properties such as C_L, C_D, and C_M were calculated over a range of angles of attack. A single test flight showed the glider pitching up until it stalled and then pitching down rapidly. The lift curve slope showed lift hysteresis due to the fast pitch rate. Data presented in the paper showed a number of flights with a detailed aerodynamic analysis of one flight.

Another investigation looked at aerodynamic modeling in the post stall region in order to achieve autonomous perching.[3,4] The researchers wanted to achieve reliable, precise perching of an unpowered fixed wing glider which required an accurate aerodynamic model. Gathering data from many test flights, a model of lift and drag was built from -20 to 140 degrees angle of attack. The model allowed them to control the 90-g (3.17-oz) glider via the elevator over a large range of angles of attack, and plan and execute a high angle of attack perching maneuver.

Other researchers gathered experimental data from human pilots remotely flying small UAVs in order to achieve autonomonous hover.[5,6] This data was used to model and then develop controllers to achieve autonomous hover. Both researchers achieved autonomous control of small UAVs by building experimentally based models of the aerodynamics over a range of angles of attack. Frank, et al.[6] built a particularly complete model that included a number of important propeller effects that were significant when the aircraft was in hover. Other have also investigated the autonomous hovering of small UAVs.[7,8]

To gather the in-flight data from aircraft, traditionally, on-board sensors have been used.[7,9,10] However, due to size and weight constraints, micro-UAVs have required off-board measurement. The most widely used off-board measurement approach has been a set of cameras that can track objects based on triangulation. A multiple infrared camera system built by Vicon has been widely used in the motion capture field and has also been used by robotics researchers.[11] Many micro-scale UAV researchers, including some of previously discussed work, have used the Vicon system to provide accurate positioning data.[1–4]

The Vicon camera system has been used to track and control small and micro-UAVs in an indoor environment. The data from the system has been used to control many different small aircraft because it offers

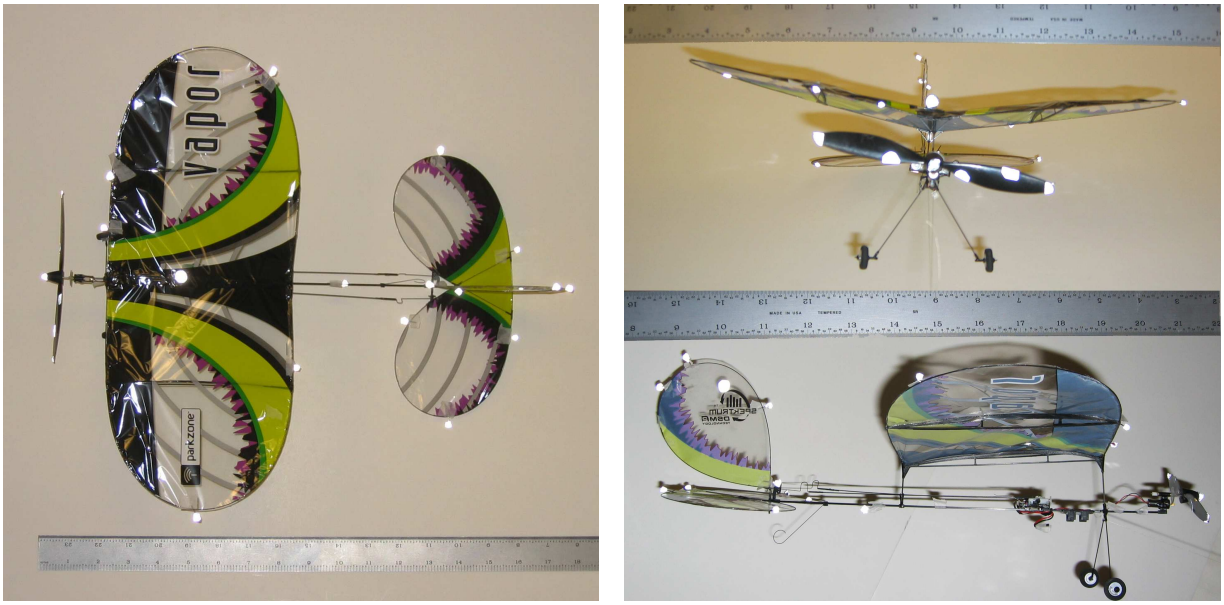

(a) The top view of the test aircraft showing the reflective markers.

(b) The front view and side view of the test aircraft showing the reflective markers.

Figure 1. The Vapor airplane with the attached reflective markers.

flexibility of quickly attaching lightweight markers. Vicon systems have been used to pursue many controls problems including implementing new controllers and researching multi-agent control using fleets of small scale helicopters.[6,12–15]

For this research, a system with eight infrared cameras built by Vicon was used.[11] The cameras used infrared lights to track reflective markers placed on the airplane. By combining sets of markers to form an object, the system can track the position as well as the orientation of the aircraft as it flies through the room. The Vicon software returns the position and orientation of the airplane in the earth reference frame which can be processed to obtain the velocities and accelerations in the body-fixed frame.

A multiple camera Vicon system is capable of very accurate measurements as analyzed by Mettler, but the measurements still have noise.[2] Since the aircraft used in this research is only semi-rigid, noise in the measurements is increased by any deflections that occur in the airplane body. In order to minimize the noise, a variety of filtering techniques were used.[9] By using techniques to reduce the noise and generate accurate position data, reliable results were obtained. The resulting data set included enough information that system identification approaches could be used to calculate aerodynamic parameters.[9,10]

In this research, a fixed wing, semi-rigid 11.5-g (0.41-oz) powered airplane was tracked using an eight camera Vicon system in an indoor environment. Using the aircraft position time-history, an estimate of the aerodynamic performance of the airplane was developed. In addition, the control surfaces were tracked to provide information on their deflections throughout flight. By combining this information, a full aircraft model could be developed.

II. Experimental Apparatus

For testing, the commercially manufactured, 37.5-cm (14.75-in) wingspan 11.5-g (0.41-oz) RC Vapor airplane shown in Fig. 1 was used.[16] Carbon fiber rods are used for the airplane structure and the aerodynamic surfaces are made of a thin plastic film. The wing is a cambered airfoil without any thickness. A battery powers a small RC receiver that controls the two servos and the electric throttle. The RC receiver actuated control surfaces are an all-moving tail with a flat plate rudder and elevator. Thrust is provided by an electric motor and a propeller with a 14.0-cm (5.51-in) diameter and a pitch of 4.5-cm (1.77-in).

The geometric and inertial properties for the airplane are listed in Table 1. The moments of inertia were

Table 1. Physical Properties of the Vapor Test Airplane.

Property	Metric Measurement	Units	English Measurement	Units
m	11.5	g	7.88×10^{-4}	slugs
I_{xx}	3.70×10^{-5}	kg-m^2	2.73×10^{-5}	slugs-ft^2
I_{yy}	1.13×10^{-4}	kg-m^2	8.33×10^{-5}	slugs-ft^2
I_{zz}	1.24×10^{-4}	kg-m^2	9.16×10^{-5}	slugs-ft^2
I_{xz}	8.75×10^{-6}	kg-m^2	6.46×10^{-6}	slugs-ft^2
I_{yz}	-3.94×10^{-7}	kg-m^2	-2.91×10^{-7}	slugs-ft^2
I_{xy}	-8.42×10^{-7}	kg-m^2	-6.21×10^{-7}	slugs-ft^2
Wingspan	37.47	cm	14.75	in
Wing area	546.5	cm^2	84.7	in^2
Wing chord (at root)	15.0	cm	5.9	in
Wing camber	6.7%			
Wing incidence angle	3.0	deg		
Wing dihedral	9.5	deg		
Airplane length	38.7	cm	15.25	in
Elevator area	175.4	cm^2	27.2	in^2
Rudder area	100.0	cm^2	15.5	in^2

calculated by cutting the airplane into small sections that were weighed individually. By combining the moments of inertia and the position of the numerous (62) small pieces, the overall moments of inertia were calculated. The total mass and location of the center of gravity was calculated the same way.

Eight infrared cameras, each with its own infrared light source were used by the Vicon system. Reflective markers were attached to the airplane as shown by the white spots in Fig. 1. The cameras tracked the circular reflections in their field of view. Using multiple camera views, the Vicon software triangulated the reflections in three dimensions. A recording rate of 100 Hz was used to captured the tracking data. Figure 2 shows a screen shot of the markers making up the different airplane parts being tracked with the Vicon software.

An airplane model was built in the Vicon software by splitting it into multiple objects so different parts could be tracked when they moved separately. For each object, the earth reference position and the Euler angles were recorded. First, the fuselage and wing were combined as a single object to provide the basic airplane position and attitude information throughout the flight. Small markers (approximately 0.2-in diameter) were positioned on the leading and trailing edges of the wing and each wing tip as well as the

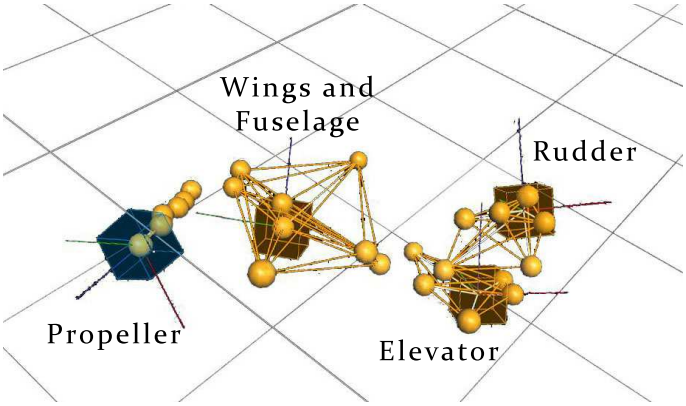

Figure 2. The Vicon markers built into separate objects with the propeller, the airplane, and the two control surfaces (left to right) being tracked in the Vicon software.

fuselage. Second, both control surfaces had sets of small markers attached so that the attitude relative to the fuselage could be calculated. Tracking data for each of the objects was recorded and later post processed to provide useful information on the airplane performance.

Two types of flight tests were conducted to gather data. Free-flight gliding tests involved hand launching the airplane without any power and included steady glides, stalls and stall recoveries. The airplane behavior could be changed by adjusting the launch speed and angle. Second, controlled glides included moving the control surfaces to investigate the effect of control surface deflections. Both types of gliding flights were constrained by the room dimensions to 2–3 sec of useful data. Gliding flights were used because the only forces acting on the airplane were from gravity and aerodynamic loads; the thrust force from the propeller was not present and did not need to be estimated. Gravity was precisely known and the aerodynamic loads were the only unknowns. By combining these different tests, a detailed model of the airplane performance could be developed. Multiple flights of each type were used to generate a rich set of data.

III. Data Acquisition and Post Processing

The data stream provided by the Vicon system included the earth reference position and the Euler angles for each of the four objects.The tracking system provided information on whether the object, that is a control surface, propeller or fuselage, was visible to the camera system and if it was, the attitude and position of the object. The tracking data from each object was filtered to acquire useful measurements.

For the fuselage object, the position and attitude were used in the post processing. The attitude, angular rates, velocities and accelerations were required to analyze the airplane performance. The first step was to transform the raw measured data from object-fixed reference frame as recorded by the tracking system to the actual center of gravity. By measuring the distance and rotation between the airplane center of gravity and the object-fixed origin, the rotation and offset between the object measured frame and the airplane center of gravity body-fixed frame was known. In order to combine the measured offsets and the earth referenced tracking data, transformation matrices were used. Each transformation matrix includes a set of angular offsets (θ_o, ϕ_o, ψ_o) and a set of position offsets (x_o, y_o, z_o) as shown below:

$$\mathbf{R} = \begin{bmatrix} \cos\theta_o \cos\psi_o & \cos\theta_o \sin\psi_o & -\sin\theta_o & x_o \\ \sin\phi_o \sin\theta_o \cos\psi_o - \cos\phi_o \sin\psi_o & \sin\phi_o \sin\theta_o \sin\psi_o - \cos\phi_o \cos\psi_o & \sin\phi_o \cos\theta_o & y_o \\ \cos\phi_o \sin\theta_o \cos\psi_o - \sin\phi_o \sin\psi_o & \cos\phi_o \sin\theta_o \sin\psi_o - \sin\phi_o \cos\psi_o & \cos\phi_o \cos\theta_o & z_o \\ 0 & 0 & 0 & 1 \end{bmatrix} \tag{1}$$

Without the position offsets, the matrix becomes a smaller three-by-three a rotation matrix about three angles and is used in later calculations. A matrix was first developed for the transformation from the airplane object measurement frame to the airplane center of gravity body-fixed frame. The resulting matrix was labeled $\mathbf{R}_{measured\ to\ CG}$. The second transformation matrix was from the earth-fixed inertial reference frame to the tracking object center that was recorded at each time step, and the matrix was labeled $\mathbf{R}_{inertial\ frame}$. By combining these two rotations through the multiplication of $\mathbf{R}_{measured\ to\ CG}$ and $\mathbf{R}_{inertial\ frame}$, the transformation from the earth-fixed reference frame to the airplane center of gravity was calculated.

$$\mathbf{R}_{ac} = \mathbf{R}_{measured\ to\ CG} \cdot \mathbf{R}_{inertial\ frame} \tag{2}$$

From the resulting R_{ac} matrix, the earth referenced attitude and position at the airplane center of gravity was determined by calculating θ, ϕ, and ψ as well as x, y, and z.

The second step was to find any time-steps in the data where the system had lost track of the object, which were usually only a few consecutive measurements during a flight. In these regions, a linear fit was used between the measurements at either side of the missing data. After filling in these few points, the noise in the raw measurements was smoothed using the Matlab implementation of the robust local regression with a 2^{nd} order polynomial.[17] The robust method was chosen because points were periodically significantly off the trend line. To find the velocity and acceleration, the smoothed data was differentiated using a 4^{th} order local fitting method developed by Klein.[9] For both the position and attitude, the same filtering techniques were used to estimate the airplane track.

From the smoothed and differentiated data, the position of the airplane along with the velocity and acceleration in the earth reference frame as well as the Euler angles were known. To transform these

quantities into a body-fixed reference frame another rotation matrix (see Eqn (1)) based on the Euler angles was used.[2,18] First the velocity and acceleration was transformed to the body-fixed frame using,

$$\mathbf{V}_b = [\ u\ v\ w\ ]^T = \mathbf{R}_{earth\ to\ body}\ \ [\ \dot{x}_E\ \dot{y}_E\ \dot{z}_E\ ]^T \tag{3a}$$

$$\mathbf{a}_b = [\ a_x\ a_y\ a_z\ ]^T = \mathbf{R}_{earth\ to\ body}\ \ [\ \ddot{x}_E\ \ddot{y}_E\ \ddot{z}_E\ ]^T \tag{3b}$$

By applying the transformations, the body-fixed axis velocity and acceleration were known. The Euler rates were calculated by transforming the Euler angular rates to the body-fixed angular rates.[2,9]

$$\begin{bmatrix} p \\ q \\ r \end{bmatrix} = \begin{bmatrix} 1 & 0 & -\sin\theta \\ 0 & \cos\phi & \sin\phi\cos\theta \\ 0 & -\sin\phi & \cos\phi\cos(\theta) \end{bmatrix} \begin{bmatrix} \dot{\phi} \\ \dot{\theta} \\ \dot{\psi} \end{bmatrix} \tag{4}$$

With all of these quantities known over the duration the flight, the analysis of the aerodynamic performance could be completed. In order to get the aerodynamic flow angles, the following two formulas were used:

$$\alpha = \arctan(w/u) \tag{5a}$$

$$\beta = \arcsin(v/V) \tag{5b}$$

The actual local flow angles remain unknown, but by assuming the air was perfectly still and ignoring the induced flow affects on the airplane, the inertial speeds used in the equations represent a good estimate of the freestream flow angles.

Forces acting on the airplane were known since the mass of the airplane stayed constant and the body-fixed axis accelerations (a_x, a_y, a_z) were known from the position tracking data. The total external forces acting on the airplane were calculated using,

$$\mathbf{F}_{external} = [\ a_x\ a_y\ a_z\ ]\ m \tag{6}$$

By subtracting the force of gravity (F_G) from the total external forces, the aerodynamic forces acting on the airplane were determined.

$$\mathbf{F}_{aero} = \mathbf{F}_{external} - \mathbf{F}_G \tag{7}$$

Three resulting components of F_{aero} were in the body-fixed axis frame and were due to aerodynamic loading on the airplane. To calculate lift and drag, which are the force components in the wind axis, the forces in the body frame needed to be transformed into the wind frame. In the literature, this has been calculated using the following formulas,

$$L = -F_z\cos\alpha + F_x\sin\alpha \tag{8a}$$

$$D = -F_z\sin\alpha - F_x\cos\alpha \tag{8b}$$

which include a small angle assumption on β in the drag calculation.[2,9] By not making a small angle approximation on the sideslip angle β in the drag calculations, the result was more accurate for a maneuvering airplane. Instead, drag was calculated using,

$$D = -F_z\sin\alpha\cos\beta - F_x\cos\beta\cos\alpha - F_y\sin\beta \tag{9}$$

which used both angles (α and β).[18] These two important quantities were calculated throughout the flight to understand the performance of the airplane.

To calculate the moments being generated by the aerodynamic loads on the airplane, a similar method to the approach used to calculate the forces was implemented. Starting with the body-fixed angular rates (p, q, and r) and the moments of inertia, the moments acting on the airplane were found using the rotational equation of motion,[2,9]

$$\frac{d(\mathbf{I}\,\omega)}{dt} = \mathbf{M}_{aero} \tag{10}$$

The airplane moments of inertia were assumed to be constant as calculated in Table 1 and the standard assumption to ignore the I_{xy} and I_{yz} was used. Those two terms could be ignored since the airplane is

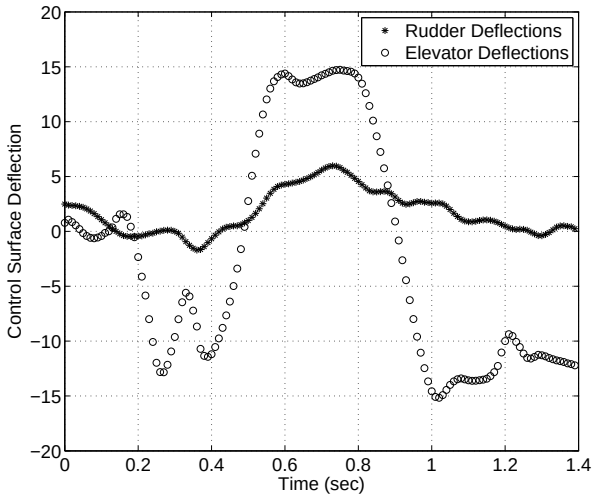

Figure 3. Experimental recorded elevator and rudder deflections.

almost symmetric about these axes and the values are very small. The moments acting on the airplane were calculated with respect to the airplane center of gravity.

$$M_x = \dot{p}\, I_{xx} - \dot{r}\, I_{xz} + q\, r\, (I_{zz} - I_{yy}) - q\, p\, I_{xz} \tag{11a}$$

$$M_y = \dot{q}\, I_{yy} + p\, r\, (I_{xx} - I_{zz}) + (p^2 - r^2)\, I_{xz} \tag{11b}$$

$$M_z = \dot{r}\, I_{zz} - \dot{p}\, I_{xz} + p\, q\, (I_{yy} - I_{xx}) + q\, r\, I_{xz} \tag{11c}$$

These three equations represent the rolling, pitching, and yawing moments being generated by the aerodynamic forces. The moments are important to understanding the response of the airplane, particularly to control surface deflections.

Through a set of calculations using the attitude and position of the airplane, the aerodynamic forces and moments were found. By knowing the aerodynamic forces and moments, the aerodynamics of the airplane could be analyzed.

A. Control Surface Deflections

In order to estimate the control surface deflections, each control surface was tracked separately. The control surface deflection is the angle between the control surface and the airplane. The attitude of the control surface, $\mathbf{R}_{cs}$, and airplane body, $\mathbf{R}_{ac}$, in the form of rotation matrices were used to find the angle between the two objects which was the deflection of the control surface. From the two rotation matrices, the rotation between the two objects was calculated using,

$$\mathbf{R}_{ac2cs} = \mathbf{R}_{ac}\, \mathbf{R}_{cs}^{-1} \tag{12}$$

to find the rotation matrix between the control surface and the airplane fuselage. Calculating the three rotation angles of $\mathbf{R}_{ac2cs}$ matrix showed that elevator deflection only affected the pitch angle between the tracked elevator attitude and the airplane attitude. The rudder deflections affected the yaw angle between the rudder attitude and the airplane fuselage attitude. Figure 3 shows the elevator and rudder deflections as recorded during a 1.40 sec test flight.

Traditionally in aircraft flight test data, the commanded or measured control surface deflections are treated as noise-free measurements.[9,10] In this case, the commanded inputs were unknown, but the actual deflections were known with noise. Since the measurements are corrupted with noise, the measured deflections of the two surfaces were smoothed in the same manner as the airplane position and attitude. By directly observing the control surface deflections and filtering the result, a good model of the control surface deflections was built and the control surface deflection time history was known throughout flight.

Table 2. The Variables Included in the Airplane State Data for Each Test.

Acceleration	a_x, a_y, a_z
Airspeed	V
Angle of attack	α
Control surface deflection	δ_e, δ_r
Drag force	D
Dynamic pressure	q
Lift force	L
Moments	M_x, M_y, M_z
Pitch, roll and yaw angles	θ, ϕ, ψ
Pitch, roll and yaw rates	p, q, r
Sideslip angle	β
Time	t
Velocity	u, v, w

B. Resulting Data Set

By processing all of the data, a complete time history of the airplane state was recorded. In order to perform a thorough analysis, a few additional variables such as atmospheric density and mass properties were measured and assumed constant throughout the testing. A list of all of the recorded and calculated variables is shown in Table 2.

IV. Results and Discussion for Lift and Drag

To illustrate the airplane performance estimated using flight test data, graphs showing some of the lift and drag aerodynamic coefficients are presented. Numerous flight tests were used to generate the graphs to minimize noise and show the overall airplane performance. Gliding flights were used for estimating the lift and drag, while controlled glides were used to study the effect of control surface deflections.

The lift and drag coefficients of the airplane during unpowered glides spanning a lower range of angles of attack are shown in Fig. 4 and 5. During each flight, the angle of attack varied as the airspeed increased and decreased due to short period oscillations and stalls. Experimental results were compared to the thin airfoil theory lift curve slope (2π per radian) corrected for a finite wing using the aspect ratio ($\mathcal{AR} = 2.04$) and the Oswald efficiency ($e_o = 0.35$).

$$C_{L_\alpha} = \frac{C_{l_\alpha}}{1 + C_{l_\alpha}/(\pi e_o \mathcal{AR})} \tag{13}$$

The Oswald efficiency factor was calculated by solving the linear fit line from both lift and drag for e_o and averaging the two results. The lift curve slope from theory was 1.65 per rad (0.0288 per deg) and is shown in Fig. 4 along with the experimental data. A least squares fit line over the angle of attack range of -5 to 25 deg is also shown and it has a slope of 1.46 per rad (0.0254 per deg) which is close to the thin airfoil theory results. Once the wing approached stall however, the thin airfoil theory is no longer valid. The drag polar is shown in Fig. 5. The total drag is a function of the parasite drag and the induced drag due to lift and it can be calculated using,

$$C_D = C_{D_o} + \frac{C_L^2}{\pi e_o \mathcal{AR}} \tag{14}$$

Figure 5 shows that the experimental data fit line matches the theoretical results during the linear portion of flight. The fit line is over a range of the C_L range of 0–1.1 and has equation of $C_D = 0.045 + 0.4\,C_L^2$. The Oswald efficiency factor, e_o, was calculated from this fit line and averaged with the result from the lift curve slope. The value of 0.35 was used to calculate the thin airfoil theory lift above as well as the thoeritical drag line. The theoretic results are also plotted in Fig. 5 and use a C_{D_o} value equal to 0.044 and the aspect ratio value of 2.04 and an Oswald efficiency factor of 0.35. The resulting equation is $C_D = 0.044 + 0.45\,C_L^2$. While

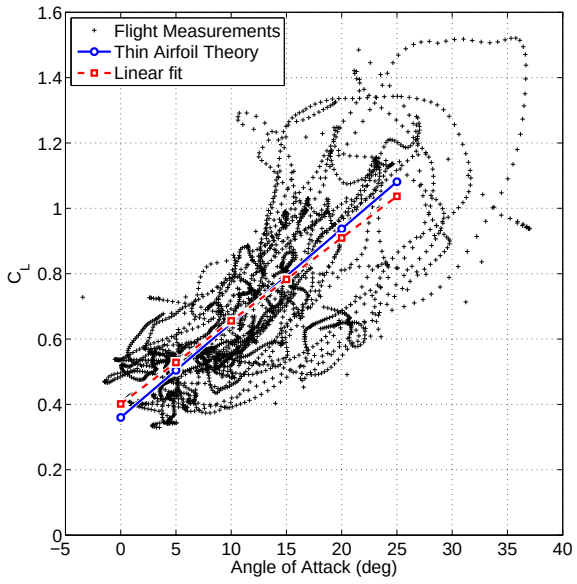

Figure 4. The experimentally measured lift coefficient compared to theoretical values at low angles of attack.

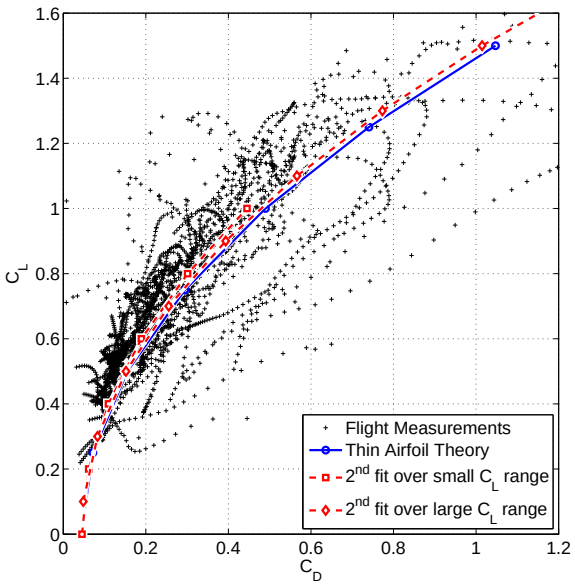

Figure 5. The experimentally measured drag coefficient compared to theoretical values at low angles of attack.

the airplane was flying at very low Reynolds numbers, approximately 20,000, the theoretical drag values still closely matched the experimental obtained values.

A second set of plots shows the lift and drag coefficients from flights over a wider range of the flight regime. When the airplane entered a stall and pitched up rapidly the airplane flew at very high angles of attack for a short time period. The results shown in Fig. 6, show the lift generated by the airplane over a range of 0–70 deg angle of attack. The previously plotted (Fig. 4) thin airfoil theory and linear fit line is also shown. As the airplane quickly pitches up, the maximum value of C_L increases temporarily to much higher values due to dynamic lift. At higher angles of attack there seem to be two distinct sets of C_L values; one at 1.5–2 and another at approximately 0.5. The stall delay (dynamic lift) due to rapid pitching motion causes the higher C_L value to occur during the pitch up motion and the decreased C_L to occur during the stall recover.

During the stalling flight, the drag coefficient continues to increase similarly to before with the lower angles of attack. During high angle of attack flight, shown in Fig. 7, the drag changes as the lift rapidly changes during stall delay. The fit line over the C_L range of 0–2.0 is $C_D = 0.044 + 0.4\,C_L^2$ which is very close to the fit line over the lower range of C_L. The drag fit model based on the flight measurements show that the theory of parasite and induced drag are applicable over a large range of values of C_L and angle of attack. Both the lift and drag measurements were close to the predicted values, but differences did exist. The differences were probably due to scaling effects that are not included in thin airfoil theory.

V. Conclusions

Using off-board tracking measurements, accurate aerodynamic parameters were estimated and used to analyze micro-scale airplane performance. Off-board measurements provided position and attitude information during airplane flights as well as control surface deflections. By combining these measurements, a full time history of the flight was developed with complete state information which was used to calculate important parameters such as the lift, drag and moments. By analyzing lift and drag, the airplane wing performance was studied. The linear response of the airplane closely matched the performance predicted by thin airfoil theory. When entering stall with a fast pitch rate, the airplane often entered a dynamic stall condition. Airplane drag coefficient over a range of angles of attack closely followed the predicted values.

Techniques developed here can easily be applied to any small remotely piloted airplane being tracked by

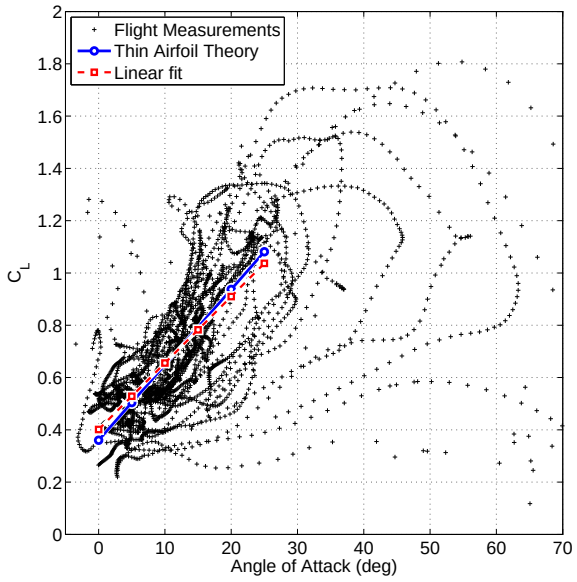

Figure 6. The experimentally measured lift coefficient compared to theoretical values over a large range of angles of attack.

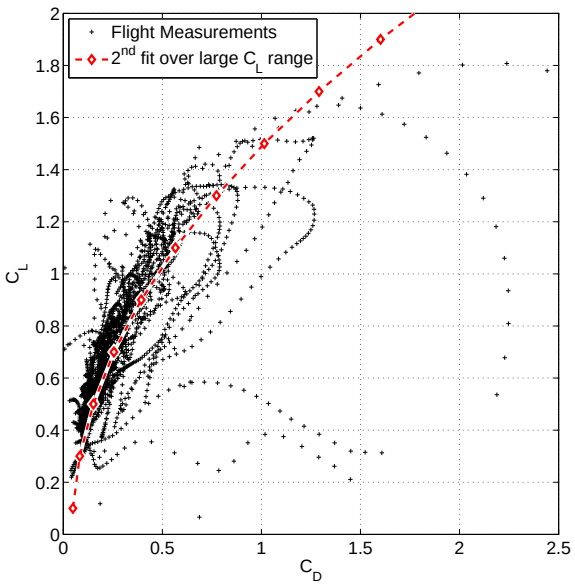

Figure 7. The experimentally measured drag coefficient compared to theoretical values over a large range of angles of attack.

off-board sensors. The position and attitude track provided an accurate time history that can be transformed into important airplane performance parameters as presented in this paper.

Acknowledgments

The authors would like to thank Or Dantsker for his piloting skill and for helping with the airplane.

References

[1]Rhinehart, M. and Mettler, B., "Extracting Aerodynamic Coefficients using Direct Trajectory Sampling," AIAA Paper 2008-6899, 2008.

[2]Mettler, B., "Extracting Micro Air Vehicles Aerodynamic Forces and Coefficients in Free Flight Using Visual Motion Tracking Techniques," *Experiments in Fluids*, February 2010.

[3]Hoburg, W. and Tedrake, R., "System Identification of Post Stall Aerodynamics for UAV Perching," AIAA Paper 2009-1930, 2009.

[4]Cory, R. and Tedrake, R., "Experiments in Fixed-Wing UAV Perching," AIAA Paper 2008-7256, 2008.

[5]Blauwe, H. D., Bayraktar, S., Feron, E., and Lokumcu, F., "Flight Modeling and Experimental Autonomous Hover Control of a Fixed Wing Mini-UAV at High Angle of Attack," AIAA Paper 2007-6818, 2007.

[6]Frank, A., McGrew, J. S., Valentiz, M., Levinex, D., and How, J. P., "Hover, Transition, and Level Flight Control Design for a Single-Propeller Indoor Airplane," AIAA Paper 2007-6318, 2007.

[7]Johnson, E. N., Turbe, M. A., Wu, A. D., Kannan, S. K., and Neidhoefer, J. C., "Flight Test Results of Autonomous Fixed-Wing UAV Transitions to and from Stationary Hover," AIAA Paper 2006-6775, 2006.

[8]Green, W. and Oh, P., "A Fixed-Wing Aircraft for Hovering in Caves, Tunnels, and Buildings," *Proceedings of the 2006 American Control Conference*, 2006.

[9]Klein, V. and Morelli, E. A., *Aircraft System Identification: Theory and Practice*, AIAA Education Series, AIAA, Reston, VA, 2006.

[10]Jategaonkar, R. V., *Flight Vehicle System Identification: A Time Domain Methodology*, AIAA Progress in Astronautics and Aeronautics, AIAA, Reston, VA, 2006.

[11]Vicon, "Vicon MX System," webpage: http://www.vicon.com/products/viconmx.html, Jan. 2010.

[12]Sobolic, F. M. and How, J. P., "Nonlinear Agile Control Test Bed for a Fixed-Wing Aircraft in a Constrained Environment," AIAA Paper 2009-1927, 2009.

[13]How, J. P., "Multi-Vehicle Flight Experiments: Recent Results and Future Directions," *Proceedings of the Symposium on Platform Innovations and System Integration for Unmanned Air, Land and Sea Vehicles*, 2007.

[14]Paley, D. A. and Warshawsky, D. S., "Reduced-Order Dynamic Modeling and Stabilizing Control of a Micro-Helicopter," AIAA Paper 2009-1350, 2009.

[15]Ducard, G. and D'Andrea, R., "Autonomous Quadrotor Flight Using a Vision System and Accommodating Frames Misalignment," *IEEE International Symposium on Industrial Embedded Systems*, 2009.

[16]E-Flite, "Vapor RTF," http://www.e-fliterc.com/Products/Default.aspx?ProdID=pkz3300, Accessed June 2010.

[17]MATLAB, *Curve Fitting Toolbox™ 2 Users Guide*, The Mathworks Inc, Natick, MA, March 2010.

[18]Stevens, B. L. and Lewis, F. L., *Aircraft Control and Simulation*, Wiley-Interscience, New York, NY, 2003.